Research paper

Magnetic field strength improvement for Lorentz actuation of a μ-Coriolis mass flow sensor

T.V.P. Schut[a,*], Y.P. Klein[a], R.J. Wiegerink[a], J.C. Lotters[a,b]

[a] MESA+ Institute for Nanotechnology, University of Twente, Enschede, The Netherlands
[b] Bronkhorst High-Tech BV, Ruurlo, The Netherlands

A B S T R A C T

In this paper we present and compare three different magnet configurations for Lorentz actuation of a μ-Coriolis mass flow sensor. The first configuration consists of 2 cylindrical magnets, the second is based on a Halbach ring, and the third configuration consists of a single cubic magnet. The magnetic field strength of each configuration is simulated. The Halbach configuration shows a magnetic field strength of 0.3 T, the single cubic configuration reaches 0.25 T. The two cylindrical magnets have the lowest field with 0.05 T. The stray field is significantly lower for the Halbach configurations compared to the other two configurations. All configurations were used for Lorentz actuation of a μ-Coriolis mass flow sensor and the frequency response was measured. The magnitude transfer between the actuation and induction voltages for the cubic and Halbach configurations show a transfer around 26 dB higher than the cylindrical configuration. The phase transfers for the Halbach and Cubical configurations are according to simulation. For the cylindrical configuration, the EMF signal is too weak to overcome the crosstalk between the actuation and induction voltages.

1. Introduction

Haneveld et al. [1] first presented a magnetically actuated μ-Coriolis mass flow sensor, as opposed to electro-statically actuated μ-Coriolis devices presented by Enoksson et al. [2] and Sparks et al. [3]. The operation principle is shown in Fig. 1. The sensor consists of a rectangular channel loop. The channel is fixed at the in-/outlet channel sections, as depicted in the figure. Conventionally, the sensor is brought into resonance by feeding a current i through a metal track on top of the channel. Lorentz forces are generated in the sections of channel perpendicular to a magnetic field **B**. These forces induce displacement of the channel. An induction voltage is generated on a second metal track. The two tracks are connected through a closed amplification loop which brings the sensor into resonance in the *Twist* mode with actuation angle θ_a (Fig. 1a). When a fluid flows through the micro-channel with a mass flow rate ϕ_m, Coriolis forces are induced in the channel section as indicated in Fig. 1. This causes additional vibration in the *Swing* mode with detection displacement Δz_d (Fig. 1b). The ratio $\Delta \hat{z}_d / \hat{\theta}_a$ is a measure for the flow. Additionally, one can obtain the density of the fluid flowing though the channel from the actuation resonance frequency.

Groenesteijn et al. [4] have presented improved magnet configurations for actuation of a μ-Coriolis mass flow sensor. Miniature magnets are placed on-chip and with their magnetic poles all in the

same direction. This showed improved field strengths but has large disadvantages, since magnets have to be somehow mounted on-chip without damaging the sensor device itself and/or without detaching over time. In this paper, new magnet configurations are presented which give a large increase in the generated magnetic field strength. Three configurations have been chosen and compared. The first uses the field between two parallel cylindrical magnets, the second uses the field in close proximity to a cubic magnet and the third uses the field within a Halbach ring based configuration. The Halbach configuration is a special magnet arrangement which reduces the stray field while enhancing the field at the ring-center. The Halbach magnet configuration has been invented by K. Halbach [5,6] and is still used today, e.g. for several machines [7] or mobile NMR applications [8].

2. Methods

2.1. Device & fabrication

The μ-Coriolis mass flow sensor used during the measurements presented in this paper was fabricated by Surface Channel Technology (SCT) [9,10]. A simplified schematic representation of the fabrication process is displayed in Fig. 2. First, a layer of low-stress silicon-rich silicon nitride (SiRN, Thickness: 500 nm) is deposited on a Silicon wafer

---

* Corresponding author.
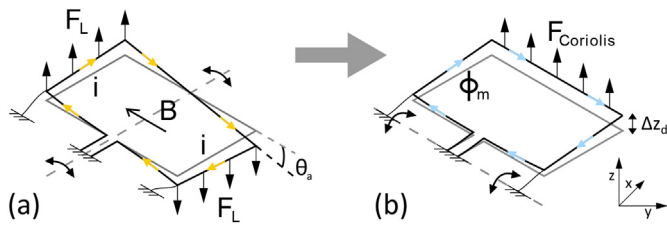 *E-mail address:* t.v.p.schut@utwente.nl (T.V.P. Schut).

Fig. 1. Operation principle of a μ-Coriolis mass flow sensor. (a): The channel loop is brought into resonance in the *Twist* mode through Lorentz force F_L resulting from a magnetic field B and a varying current i. (b): A mass flow ϕ_m through the channel induces vibration in the *Swing* mode through Coriolis force $F_{Coriolis}$.
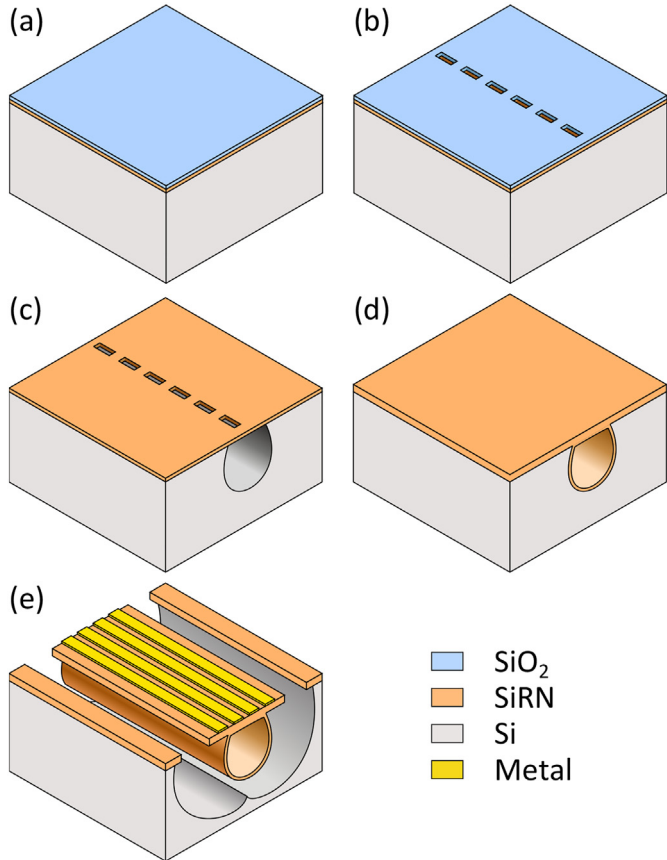

Fig. 2. Fabrication process for *Surface Channel Technology*. (a): Silicon wafer with 500 nm SiRN and 500 nm SiO₂. (b): Patterning of slit openings. (c): Removal of SiO₂ hard mask and forming of the surface channel. (d): Closing of the channel. (e): Patterning of metal and release of the channel.
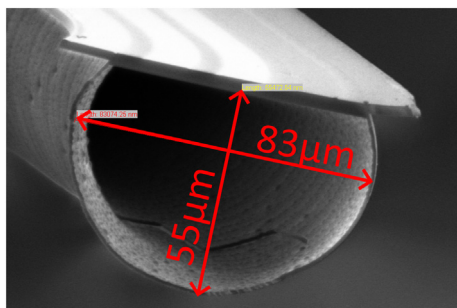

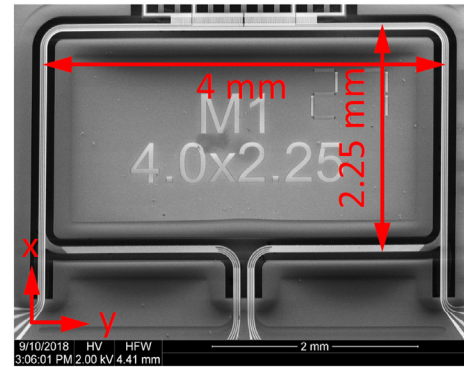**Fig. 3.** Typical cross-section of a'Surface Channel' [?].

Fig. 4. SEM image of the sensor type used for all simulations and measurements in this paper.

by Low-Pressure Chemical Vapour Deposition (LPCVD), see Fig. 2a. On top of this, a layer of silicon di-oxide (SiO₂) is deposited (LPCVD, Thickness: 500 nm), serving as a hard mask. Slits of 5×2 μm are etched through both layers by plasma etching, see Fig. 2b. Then the layer of SiO₂ is removed and a channel is formed by semi-isotropically etching silicon through the slits, see Fig. 2c. This is done by plasma etching as well. The channel is closed by conformally depositing another layer of low-stress SiRN, see Fig. 2d. Metal tracks are patterned on top of the channel (Fig. 2e), these are used for actuation and readout of the sensor. Following this, openings are etched through the nitride and finally the channel is released by isotropic etching of silicon by an SF₆ plasma. A typical cross-section of a surface channel made by this technology is displayed in Fig. 3.

Fig. 4 shows an SEM image of the sensor. Multiple metal tracks can be seen on the channel, a.o. for capacitive readout and temperature measurement. In this paper only two metal tracks are actually used: one to provide the current for actuation of the sensor and one for measurement of the induction voltage generated by vibration of the channel.

2.2. Frequency response

As described earlier, the μ-Coriolis mass flow sensor is actuated by means of Lorentz forces. Fig. 5 shows a schematic representation of the sensor and closed amplification loop which is used to bring it into resonance. There are two metal tracks on top of the microfluidic channel of the sensor. An actuation voltage v_{act} is supplied to one track. Due to vibration of the channel, an electromotive force (EMF) is generated on the other track. This EMF (v_{EMF}) is then fed into an amplifier circuit. The amplified signal is fed back to the actuation track of the sensor. This closed loop circuit drives the sensor into resonance.

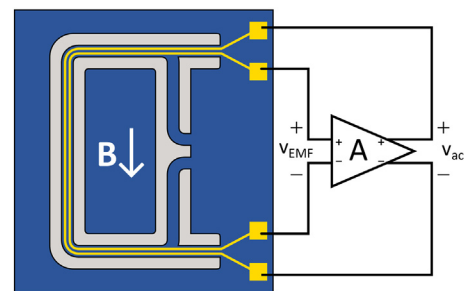The vibrations of the sensor during actuation can be described by a second order differential equation:

Fig. 5. Schematic representation of the actuation loop which is used to bring the Coriolis flow sensor into resonance. Where v_{EMF} is the generated electromotive force and v_{act} is the actuation voltage used to generate Lorentz forces in combination with a magnetic field **B**.

$$J\theta''(t) + R\theta'(t) + S\theta(t) = \tau_{\text{ext}}(t) \tag{1}$$

where J is the moment of inertia, R is the damping coefficient, S is the torsional spring constant, $\tau_{\text{ext}}(t)$ is the external torque induced by Lorentz forces and $\theta(t)$ is the actuation mode angle (see Fig. 1). $\tau_{\text{ext}}(t)$ can be expressed as:

$$\tau_{\text{ext}}(t) = \frac{BLd}{R_{\text{track}}} \cdot v_{\text{act}}(t) \tag{2}$$

where B is the magnetic field strength, L is the length of metal track where Lorentz forces are generated, d is the distance between these track sections and R_{track} is the resistance of the metal track. The induction voltage generated on the second metal track is dependent on the velocity of the channel in the z direction:

$$v_{\text{EMF}} = 2BL \cdot z'(t) \tag{3}$$

This can then be related to the the actuation angle θ (for small value of θ):

$$z(t) = \frac{d}{2} \cdot \sin(\theta(t)) \approx \frac{d}{2}\theta(t) \tag{4}$$

$$\begin{aligned} V_{\text{EMF}}(\omega) &= 2BL \cdot j\omega Z(\omega) \\ &= BLd \cdot j\omega\theta(\omega) \end{aligned} \tag{5}$$

$$\theta(\omega) = \frac{V_{\text{EMF}}(\omega)}{j\omega BLd} \tag{6}$$

Now converting Eq. (1) to the frequency domain and substituting Eqs. (2) and (6):

$$\begin{aligned} J(j\omega)^2\theta(\omega) + Rj\omega\theta(\omega) + S\theta(\omega) &= \tau_{\text{ext}}(\omega) \\ \theta(\omega) \cdot ((j\omega)^2 J + j\omega R + S) &= \frac{BLd}{R_{\text{track}}} \cdot V_{\text{act}}(\omega) \\ \frac{V_{\text{EMF}}(\omega)}{j\omega BLd} \cdot ((j\omega)^2 J + j\omega R + S) &= \frac{BLd}{R_{\text{track}}} \cdot V_{\text{act}}(\omega) \end{aligned} \tag{7}$$

Finally, the transfer function from V_{act} to V_{EMF} becomes:

$$\begin{aligned} \frac{V_{\text{EMF}}}{V_{\text{act}}} &= \frac{j\omega B^2 L^2 d^2}{R_{\text{track}} \cdot ((j\omega)^2 J + j\omega R + S)} \\ &= \frac{j\omega B^2 L^2 d^2 / S}{R_{\text{track}} \cdot \left(1 + j\frac{\omega}{\omega_0}\frac{1}{Q} + \left(j\frac{\omega}{\omega_0}\right)^2\right)} \end{aligned} \tag{8}$$

where ω_0 is the resonance frequency and Q is the quality factor:

$$Q = \frac{\sqrt{SJ}}{R} \tag{9}$$

$$\omega_0 = \sqrt{\frac{S}{J}} \tag{10}$$

Eq. (8) is used in combination with the simulated magnetic field strengths to generate simulated transfer curves for the various magnet configurations. These are compared with transfer curves measured using a gain-phase analyser. The measurement setup is effectively as shown in Fig. 5 where the amplifier circuit is then substituted by an HP 4194A gain-phase analyser.

2.3. Magnetic simulation and assembly

Three different magnet configuration have been simulated and measured.

The simulations have been done using CADES simulation software, entirely described by Delinchant et al. [11]. Magnetic interactions are modelled with the MacMMems tool, which uses the Coulombian equivalent charge method to generate a semi-analytic model. This model is used by the CADES framework (component calculator, component optimizer) to calculate the designs.

Three different magnet configurations have been simulated and measured as shown in Fig. 6.

The cylindrical configuration consists of two cylindrical, axially

magnetized magnets (radius: 3 mm, length: 13 mm, material: NdFeB N42, obtained from www.supermagnete.nl) arranged parallel with a distance of 19 mm between them. The chip has been placed in the middle with an offset of 3 mm in the z-direction, as shown in Fig. 6a. Our Halbach-ring (Fig. 6b) consists of 8 magnets (material NdFeB N45, obtained from www.supermagnete.nl). 4 of them, placed in the corners, cubic with an edge length of 7 mm, the other ones are 7 mm × 7 mm × 14 mm. The cubic configuration (Fig. 6c) consists of a cubic magnet with an edge length of 12 mm (material NdFeB N45, obtained from www.supermagnete.nl) placed parallel, directly above the chip. In all configurations the channels of interest have a length of 2.25 mm and are located at y = −2 mm and 2 mm. The magnets can be placed in a holder surrounding the chip allowing for simple plug and play operation.

3. Results and discussion

The magnetic field strength of three different magnet configurations have been simulated. For all configurations the y-field shows a uniform profile along the channel, see Fig. 7. The Halbach configuration reaches a strength 0.3 T, the single cuboid configuration 0.25 T. The cylindrical configuration has the lowest field with 0.05 T.

The x-field of the Halbach and Cube configuration shows a slope of −0.01 T/mm, the cylinder −0.003 T/mm, see Fig. 8. The slope of each configuration scales with the reached absolute field. The field is antisymmetric around $x = 0$ due to symmetry of the magnet configurations. This means additional Lorentz forces are generated in the channel section perpendicular to the y-axis. Due to the anti-symmetry of the x-field this will cause additional vibration in the actuation mode. The Coriolis mode is unaffected by this field.

The stray magnetic field strengths of the three configurations were simulated at a distance of 10 mm from the outer magnet surface, see Table 1. The Halbach configuration shows the lowest stray field strength of 0.006 T, compared to 0.025 T for the cylindrical configuration and 0.081 T for the cubic configuration.

The magnitude and phase transfer between the actuation voltage v_{act} and induction voltage v_{EMF} was measured (as described in Section 2.2) for the three magnet configurations in Fig. 6. The magnitude and phase transfer are displayed in Fig. 9a and b respectively. The analytical curves are generated using Eq. (8) in combination with the simulated magnetic field strengths for the three configurations (see Fig. 7). For both figures the x-axis is centered around the resonance frequency, which lies around 3.8 kHz varying slightly with temperature, pressure and from chip to chip.

The measured magnitude transfers for the 3 configurations are; Halbach: −59.1 dB, Cubic: −58.0 dB, Cylindrical: −84.6 dB. As expected, both the Halbach and single cube configuration show a higher magnitude transfer than the cylindrical configuration, around 26.5 dB. For the cubic configuration, this corresponds well with the analytical curve. The measured value is slightly higher than simulated. This could be due to deviation of the position of the magnet along the z-axis where it is actually closer to the sensor chip than simulated. Other causes could be a deviation in the quality factor or resonance frequency of the Coriolis flow sensor. For the Halbach configuration, the simulated value of the magnitude transfer lies 4.4 dB higher than the measured value. This is most likely due to misalignment of the magnets in the Halbach configuration. Since the fields of the magnets in the configuration oppose each other, it is difficult to accurately place and align them. Misalignment of the sensor chip to the centre of the magnets along the z-axis (where the magnetic field is the strongest) could be another cause of the lower measured transfer.

The phase transfer of all the configurations should in principle be a curve going from +90 to −90°, eventually going back to +90° due to cross-talk via parasitic capacitance between the actuation and induction tracks. At resonance, the phase shift should be 0°. However, since the signal in case of the cylindrical configuration is so small, the phase shift
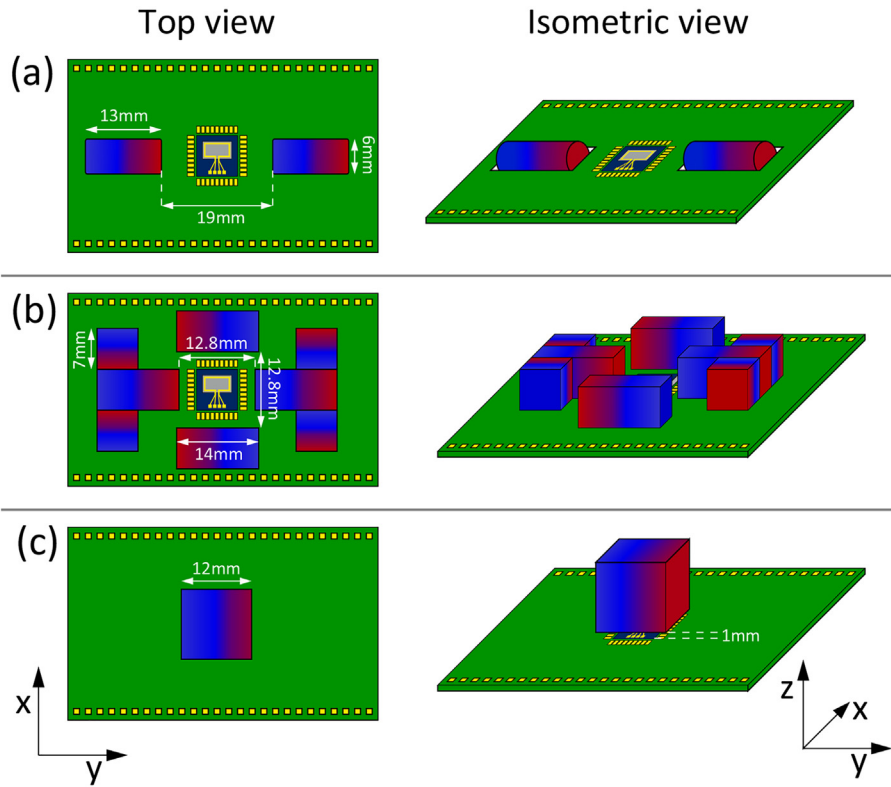
Fig. 6. μ-Coriolis sensor chip on PCB with different magnet configurations. a) Conventional 13 × 6 mm cylinder magnets, b) Halbach configuration with cube magnets with sides of 7 mm. c) Single large 12 mm cube magnet. Red and blue indicate the north and south pole of the magnets respectively. (For interpretation of the references to color in this figure legend, the reader is referred to the web version of this article.)
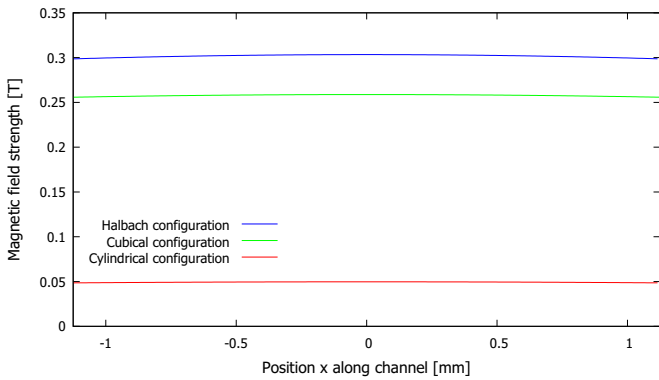

Fig. 7. Simulated magnetic field strength in the *y*-direction along the side 2.25 mm channel section (Fig. 4). Halbach configuration (blue) shows the highest field strength (0.3 T) followed by the single cubic magnet (green), arranged on top of the chip (0.25 T). Using two cylindrical magnets (red) results in a field strength of 0.05 T. (For interpretation of the references to colour in this figure legend, the reader is referred to the web version of this article.)
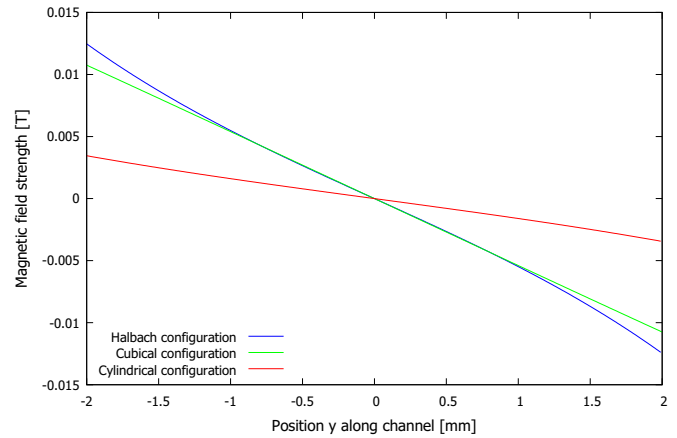
is heavily affected by cross-talk (see Fig. 9b). The phase shift does not even reach 0°. The EMF signal is too small to overcome the cross-talk via parasitic capacitance between the two metal tracks. We can see a similar effect in the magnitude transfer of the cylindrical configuration where the resonance peak barely reaches out above the noise floor. To stably bring the sensor into resonance, it is critical that this 0° point can be detected. For the other two configurations, the phase transfer is as expected. For these, the sensor should be able to be brought stably into resonance with an amplification loop with relatively low gain. This can enhance the signal-to-noise ratio of the overall sensor. Especially for fluid density measurements this can improve the accuracy significantly, since the resonance frequency is directly related to the density of the fluid flowing though the channel.

Fig. 8. Simulated magnetic field strength in the *x*-direction along the top 4 mm channel section (Fig. 4). All configurations show a linear gradient of the *x*-field along the channel. The Halbach and Cube configuration have slope of −0.01 T/mm, the cylinder −0.003 T/mm.

Table 1
Stray magnetic field strength along *y*-axis of the three configurations at a distance of 10 mm from the outer magnet surface.

Configuration	Stray field [T]
Cylindrical	0.025
Halbach	0.006
Cube	0.081

4. Conclusion

The Halbach configuration shows the highest simulated field strength (0.3 T) followed by the single cubic magnet (green) positioned
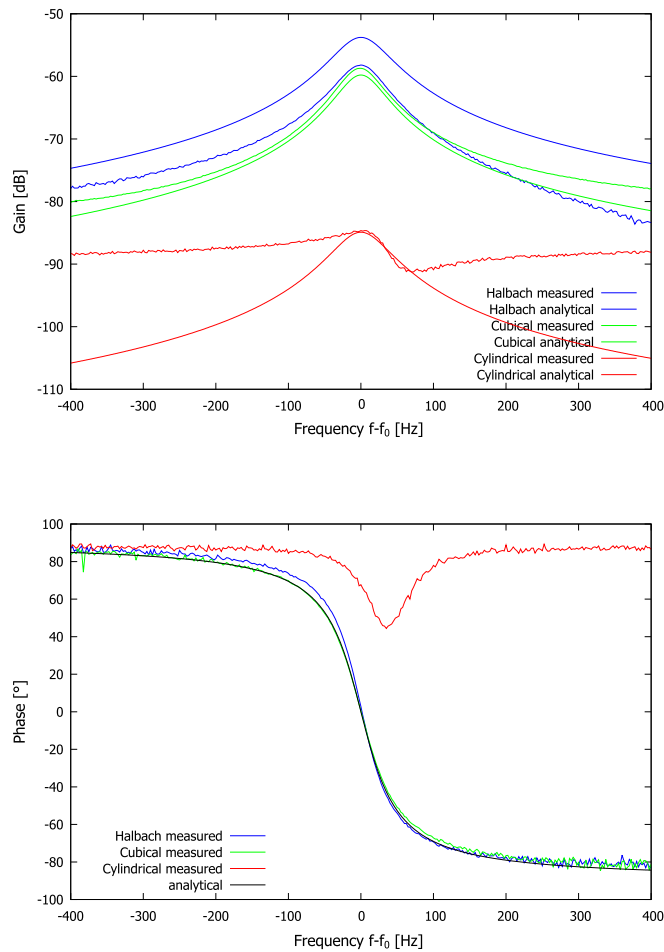
Fig. 9. Magnitude and phase transfers between the actuation voltage v_{act} and induction voltage v_{EMF}.

above the chip (0.25 T). Two cylindrical magnets (red) generate a field strength of 0.05 T, see Fig. 7. All configurations show a linear gradient of the x-field along the channel. The Halbach and Cube configurations have a slope of -0.01 T/mm and the cylindrical configuration shows a slope of -0.003 T/mm. Both the cubic and cylindrical configurations show a constant z-field offset (-0.115 T & -0.01 T respectively) along the channel, the Halbach configuration shows no offset (Fig. 8). The Halbach configuration shows the lowest stray field, see Table 1.

Magnitude transfer measurements between the actuation and induction voltages for the cubic and Halbach configurations show a transfer 26 dB higher than the cylindrical configuration, see Fig. 9a. Phase transfer measurements show that the Halbach and cubic

configurations generate transfer plots according to simulation. The low EMF signal amplitude for the cylindrical configuration causes the phase to only reach down to 45° before going back up to 90°. This means the Halbach and cubic configurations are more suitable for use with an amplification loop to bring it into stable resonance, which is important for overall performance of the μ-Coriolis flow sensor. To conclude, the Halbach configuration has the most promising results regarding its field strength and stray-field but is hard to assemble due to the repelling forces of the magnets. Therefore we would suggest to use a single large cubic magnet which combines a high magnetic field and a practical way to assemble the final sensor.

Declaration of Competing Interest

None.

Acknowledgements

References

[1] J. Haneveld, T.S.J. Lammerink, M.J. de Boer, R.G.P. Sanders, A. Mehendale, J.C. Lötters, MDijkstra, and R.J.Wiegerink. Modeling, design, fabrication and characterization of a micro coriolis mass flow sensor, J. Micromech. Microeng. 20 (12) (2010) 125001.

[2] P. Enoksson, G. Stemme, E. Stemme, A silicon resonant sensor structure for coriolis mass-flow measurements, J. Microelectromech. Syst. 6 (2) (1997) 119–125.

[3] D. Sparks, R. Smith, J. Cripe, R. Schneider, N. Najafi, A portable mems coriolis mass flow sensor, IEEE SENSORS, 2003, pp. 337–339.

[4] J. Groenesteijn, T.S.J. Lammerink, R.J. Wiegerink, J. Haneveld, J.C. Lötters, Optimization of a micro coriolis mass flow sensor using Lorentz force actuation, Sensors Actuators A Phys. 186 (2012) 48–53.

[5] K. Halbach, Strong rare earth cobalt quadrupoles, IEEE Trans. Nucl. Sci. 26 (3) (jun 1979) 3882–3884.

[6] K. Halbach, Design of permanent multipole magnets with oriented rare earth cobalt material, Nucl. Inst. Methods 169 (1) (1980) 1–10.

[7] H. Raich, P. Blümler, Design and construction of a dipolar halbach array with a homogeneous field from identical bar magnets: NMR mandhalas, Concepts Magn. Reson. Part B: Magn. Reson. Eng. 23B (1) (oct 2004) 16–25.

[8] Z.Q. Zhu, D. Howe, Halbach permanent magnet machines and applications: a review, IEE Proc. Electric Power Appl. 148 (4) (2001) 299.

[9] J. Groenesteijn, M.J. de Boer, J.C. Lötters, R.J. Wiegerink, A versatile technology platform for microfluidic handling systems, part i: fabrication and functionalization, Microfluid. Nanofluid. 21 (7) (2017) 127.

[10] J. Groenesteijn, M.J. de Boer, J.C. Lötters, R.J. Wiegerink, A versatile technology platform for microfluidic handling systems, part ii: channel design and technology, Microfluid. Nanofluid. 21 (7) (2017) 126.

[11] B. Delinchant, D. Duret, L. Estrabaut, L. Gerbaud, H. Nguyen Huu, B. Du Peloux, H.L. Rakotoarison, F. Verdiere, F. Wurtz, An optimizer using the software component paradigm for the optimization of engineering systems, COMPEL 26 (2) (2007) 368–379.